Pressure-dependent topographic evolutions of cold–sintered zinc oxide surfaces

Journal:	*Journal of Materials Chemistry C*
Manuscript ID	TC-COM-09-2021-004651.R1
Article Type:	Communication
Date Submitted by the Author:	24-Oct-2021
Complete List of Authors:	Bang, Sun Hwi; The Pennsylvania State University, Materials Research Institute Randall, Clive; The Pennsylvania State University, Materials Research Institute

SCHOLARONE™
Manuscripts

Journal of Materials Chemistry C

COMMUNICATION

Pressure-dependent topographic evolutions of cold-sintered zinc oxide surfaces

Sun Hwi Bang,[*a] and Clive A. Randall[a]

By applying atomic force microscope to the flat in-plane polycrystalline microstructure, pressure-dependent topographic evolutions can be studied with respect to surface dihedral angle and groove geometry. Using cold-sintered zinc oxide densified at 200°C as a model system, this study demonstrates an experimental methodology for quantification of relative grain boundary energetics in cold-sintered materials system and an associated geometric model for connecting the morphological change and underlying mechanochemical phenomenon under various uniaxial pressures ranging from 70 to 475 MPa. Depending on the applied pressure, anisotropic grain growth, normal grain growth, and coarsening are distinctively observed according to the changes in the groove geometry, suggesting that the growth kinetics is can be considered as a function of pressure.

Zinc oxide (ZnO) is a versatile material used in a wide range of functional applications and existed in various sizes and forms.[1,2] This n-type semiconductor material has a melting point of 1975°C,[3] indicating that high sintering temperature is necessary to densify into a bulk and polycrystalline form. However, the recent advances in cold sintering process has revealed that ZnO and other material systems can be highly densified at substantially low temperature.[4–6] Considering that the homologous temperature of solid-state sintering is generally around 0.70 to drive atomic diffusion, the cold sintering only requires 0.20 or below to enable a powder densification. Such a low-temperature process is governed by dissolution and precipitation enabled by a transient liquid phase under uniaxial pressure and heat, where its mechanochemical process closely resembles the diffusive mass

transfer of pressure solution creep.[7,8] In fact, the time scale of the cold sintering is radically faster than the length of the geologic phenomenon but fluid-enhanced dissolution at grain contacts and precipitation at pore comparably occur in both processes.

Innovating a low-temperature sintering is directly related to reduce environmental footprint and also opens new opportunities in materials discovery.[9,10] Although the research, technological and societal values of the cold sintering process have been comprehensively elucidated and resonated among diverse scientific communities, understanding of its fundamental sintering mechanism is rather limited especially in associated mechanochemical evolutions[11] and localized characterizations.[12] Hence, this study proposes 1) a method of preserving in-plane surface (perpendicular to the axial direction) microstructure to characterize the topographic evolutions of cold-sintered ZnO and 2) an associated geometric model to understand the surface morphological change with respect to uniaxial pressure. Moreover, the accurate measurements of the dihedral angle between grain contacts are unique attributes, which can be used for understanding grain growth, anisotropic energetics, and microstructural dimensionality.[13] Although the proposed technique is limited to capturing the surface microstructural features, which may be possibly different from the inside, it indeed provides unexplored insight into the cold sintering process and even enables the characterizations of localized phenomena at ceramic and ceramic composite grain boundary.

Methods

Cold sintering process. ZnO (Alfa Aesar 40 – 100 nm APS powder) and transient chemistry of 2 M acetic acid solution were cold-sintered for 60-minutes of isothermal dwell at 200°C after average heating rate of 15°C min^{-1} under various hydraulic uniaxial pressures (70, 205, 340, and 475 MPa). The detailed experimental procedure is described in the previously reported work.[14] To obtain a very flat in-plane surface for atomic force microscope (AFM) measurement, a finely polished inconel disk (Nickel Alloy 625) was inserted between the powder layer and die punch to

[a]*Materials Research Institute and Department of Materials Science and Engineering, Pennsylvania State University, University Park, PA, 16802, USA*

[*]*Email: sbang@psu.edu*
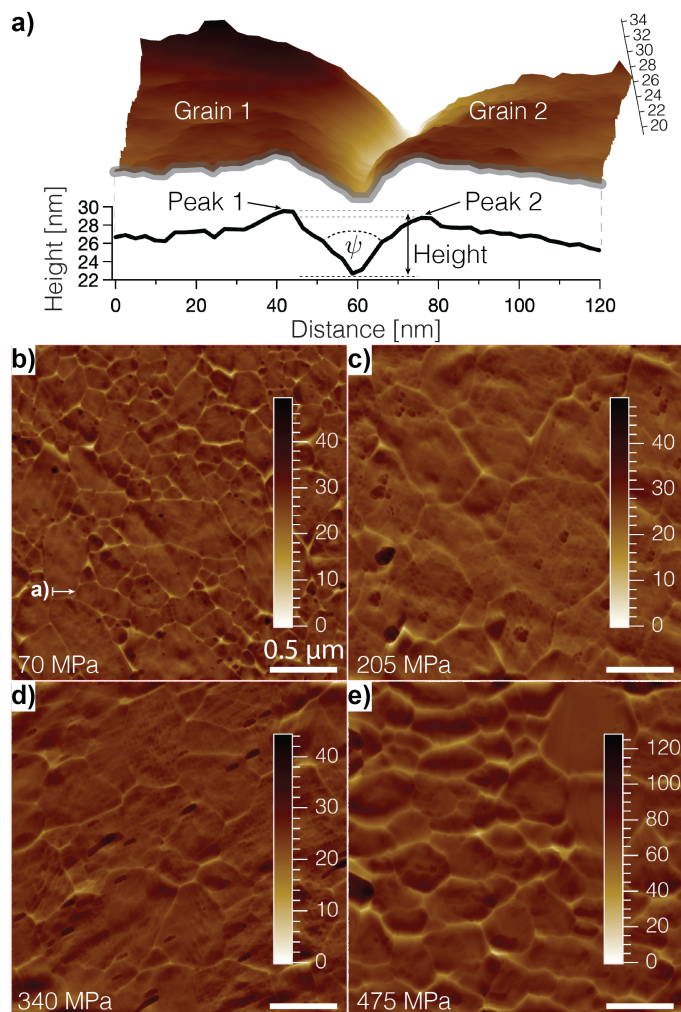
Fig. 1 AFM height measurements (nm) of the cold-sintered ZnO at 200°C for 60 minutes. a) 3D groove of adjoining grains viewed from the arrow shown on b) and the bottom plot displays the cross-section of the highlighted region, including the peak, average height, and surface dihedral angle (ψ). b–e) Various uniaxial pressures of 70, 205, 340, and 475 MPa.

Fig. 2 Topographic analysis of 550 data points at different applied pressures. a) Surface dihedral angle distributions between adjoining grains. Cumulative frequencies of b) peak-to-peak distance, c) height, and d) relative grain boundary energy using Eq.(1).

preserve the pristine microstructural features such as grain, grain boundary, and pore. Note that this proposed method does not require to use of thermal or chemical etching to reveal a grain groove and can be generally applicable to other cold sintering material systems for characterizing topographic features and localized mechanical and electronic phenomena. The commercially available inconel disk (McMaster-Carr 625 Nickel) was cut from a 3.175-mm thick sheet using electrical discharge machining and then polished using alumina suspension.

AFM characterization. AFM (Bruker Dimension Icon II) and probe (Bruker SCANASYST-AIR) were used in PeakForce tapping mode to characterize the topographies of the cold-sintered sample. After image flattening and filtering processes, topographic analysis was conducted using a custom MATLAB file (github.com/sunhwibang/AFMtopography), which takes (x, y, z) coordinates as an input and extracts the surface dihedral angle (ψ), peak-to-peak distance (d) and height (h) as an output. Then,

the ratio of the grain boundary energy (γ_{GB}) and surface free energy (γ_s) is related to ψ by using Mullins' analysis:[15]

$$\frac{\gamma_{GB}}{\gamma_s} = 2\cos\left(\frac{\psi}{2}\right) \quad (1)$$

To achieve statistically meaningful data size, 550 grain boundaries were randomly analyzed for each uniaxial pressure.

Results

Surface microstructure. Fig. 1a demonstrates an example of grain-to-grain contact of the cold-sintered ZnO by the AFM height measurement. The 3D topography clearly displays the distinction between grain and grain boundary and the roughness between two grains, which may be due to grain shape accommodation under the given cold sintering condition. On the 2D line plot, a peak is defined as the highest point seen from the valley, a height is the distance between the average peak to valley, and a dihedral angle (ψ) is the groove angle measured between two peaks. Fig. 1b–e

shows the microstructures under various uniaxial pressures. At 70 MPa, it is evident that the wide range of grain size is shown from 50 to 800 nm, indicating that the some of initial particle is still present in the microstructure while grain growth were in progress. Also, the presence of anisotropic grain is obvious, suggesting that the pressure may impact growth rate during heating and isothermal dwell (Fig. S1). This observation agrees with the previously reported study[16] in which the grain aspect ratio increases using low pressure (27 MPa). In the cases of 205 and 340 MPa, the population of the initial size is no longer observed and grain growth is rather equiaxed. It is not yet clear to understand the role of uniaxial pressure with respect to grain growth, but such pressures may improve homogeneous transient phase distribution between grain contacts, which will determine the rates of dissolution and precipitation. Regarding the surface flatness of those pressures (70 – 340 MPa), the maximum height is below 45 nm, which sufficiently captures the in-plane microstructural features without undesired distortion from surface roughness. However, when 475 MPa is used, the maximum height now increases to 125 nm, which is due to the sharp increase in height between grain contacts. As the size and shape of grain are changed to larger and faceted compared to the initial particle observed in the case of 70 MPa, the high pressure still has mechanochemical effects but the particle growth mechanism may be different from the low pressures.

Topographic analysis. Fig. 2a plots the histograms of the surface dihedral angles. For 70 and 475 MPa, a bell curve is centered around 90°C, whereas the cases of 205 and 340 MPa apparently show a negatively skewed distribution where the modes are placed between 130 and 140°C. This supports the aforementioned microstructural observations where the growth kinetics may be distinctively different based on applied pressure. Considering that two contacting spheres make a 90°C between zeniths, it can be reasonably deduced that the length of interparticle contact may be smaller in the cases of 70 and 475 MPa compared to the larger dihedral angle. Fig. 2b–c measure the cumulative frequencies of peak-to-peak distance and height. For 70 – 340 MPa, the median (50%) of the peak-to-peak distance is 24.7±1.1 nm, but the height is noticeably reduced by 60%. Then, maintaining the same groove width while shortening the height leads to a conclusion that the growth of interparticle contact is obvious for the cases of 205 and 340 MPa. Although those low pressures present a comprehensible microstructural trend between interparticle contact growth and applied pressure, the case of 475 MPa shows different growth behaviors. The corresponding median values of its width and height measurements are 60.1 and 21.8 nm, respectively. Considering all the topographic observations of the high pressure case, it is plausible that the ZnO particles are prone to a coarsening process where grain shape changes due to confined space defined by die dimension. For a case of ZnO cold sintering with acetic acid solvent, it has been widely reported that zinc acetate appears as one of the possible transient phases,[14] which can thermally decompose and recrystallize to form ZnO:

$$Zn(CH_3COO)_2 + H_2O \longrightarrow ZnO + 2CH_3COOH \qquad (R1)$$
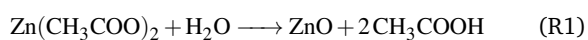
As the current study uses the sintering temperature of 200°C, it is likely that zinc acetate phase still remains in the system regarding its differential thermal analysis data.[17] Then, with the residual zinc acetate, such coarsening may share some perspectives reported in the literature.[18] Fig. 2d displays the relative grain boundary energy based on Eq. (1) and the two major median values are 0.85±0.03 and 1.34±0.01. Note that the relative grain boundary energy is equal to unity when the surface surface dihedral angle is 120°, which is the same angle observed in the 2D triple junction with isotropic energies. Table 1 summarizes topographic analysis and relative grain boundary energy of the current study and compares with other relative grain boundary energy studies using thermal etching. Comparing the normal grain growth cases of the cold-sintered ZnO (205 – 340 MPa), the peak-to-peak distance is at least one order of magnitude smaller than the thermal grooves, whereas both surface dihedral angle and relative grain boundary energy are in reasonable agreement.

Table 1 Summary of peak-to-peak distance (d), surface dihedral angle (ψ), and relative grain boundary energy (γ_{GB}/γ_s).

Material	d [nm]	ψ [°]	γ_{GB}/γ_s @ 50%
ZnO (current study)	25 – 27	128 – 131	0.82 – 0.88
Magnesia[19]	2000 – 2200	105	1.22
Alumina[20]	307 – 327	116 – 120	1.00 – 1.05
Na$_2$O$_3$-doped alumina[21]	964 – 1260	123 – 133	0.80 – 0.95
Ca-doped yttria[22]	400 – 470	156 – 164	0.28 – 0.42
YAG[23]	350 – 370	155 – 160	0.35 – 0.52

Discussions

Pressure-dependent geometric model. From the topographic analysis, it is evident that the applied pressure changes the resulting geometry of adjoining grains. In order to understand such a pressure-dependent phenomenon, it is important to know the different pressures present during a cold sintering process. When external uniaxial pressure is applied, the resulting radial die wall pressure is linearly proportional, which can be denoted by:

$$P_{radial} = KP_{axial} \qquad (2)$$

where K is the coefficient pertaining to particle compaction behaviors and its typical value is 0.46±0.04.[24] Note that these pressures have concerns in the ceramic powder, metal compaction, and pharmaceutical pill pressing. Across these different fields, there is general agreement on the presence of the uniaxial and radial pressures, where the radial component is linked to particle friction and friction from the die wall[25,26]. However, localized particle pressure can be distinctively different from those axial and radial global pressures as the Hertz contact theory is now considered to describe the stress between adjoining surfaces.[27] Also, capillary force is presented in a powder-solvent system where a thin liquid bridge can pull adjoining spheres and nano-range separation distance can result exponential force effect.[28] Hence, we recognize that both global and localized pressures are present during a course of ZnO cold sintering, but the localized pressure will be highly variable due to rapid change in particle morphology and evaporation of the transient phase, which contributes to

a thermodynamic nonequilibrium nature of the cold sintering.

Fig. 3a demonstrates the grain geometric model based on the topographic measurements. Assuming that the initial geometry of adjoining grains consists of point contact, in the case of low pressure, such a point contact evolves into a line contact due to particle coalescence, resulting in a wider dihedral angle and shorter height while peak-to-peak distance remains the same. In contrast, high pressure is more relatable to particle coarsening in a confined space where the point contact is still maintained while both height and peak-to-peak distance increase. Considering pressure-solution creep as a dominant mechanochemical reaction that drives a cold sintering process, the proposed geometric model is also explainable by its dissolution and precipitation along with the stress potential. Fig. 3b describes that solvent-enhanced dissolution occurs at grain contact and the dissolved species move along the localized pressure gradient then precipitate on the closest pore surface. Both particle coalescence and Ostwald ripening may play a key role to obtain sintering; once amorphous crystals form on the pore surface via Ostwald ripening, then those new phases recrystallize onto neighboring particles surfaces via particle coalescence to minimize interfacial free energy.[29] Fig. 3c conceptualizes the pressure-dependent sintering phenomena. Let critical pressure ($P_{critical}$) define as the minimal global pressure to drive cold sintering, this study finds that the different applied pressure does seem to have an impact on either densification or coarsening. Considering that particle coarsening is driven by Ostwald ripening,[30] it infers that high pressure accelerates Ostwald ripening where the recrystallization becomes a rate-limiting step.

Estimating absolute grain boundary energy. From the given relative grain boundary energy measurements, the absolute grain boundary energy can be estimated if surface free energy is known, which can be experimentally characterized using Young's Equation:

$$\gamma_{sv} = \gamma_{sl} + \gamma_{lv} \cos\theta \qquad (3)$$

where γ_{sv}, γ_{sl} and γ_{lv} are the interfacial surface tension between solid-vapor, solid-liquid and liquid-vapor phases, respectively. Here, θ refers to the thermodynamic equilibrium of those interfaces and it is inversely proportional to surface free energy.[31] Table 2 summarizes the wide range of ZnO surface free energies in literature as the they can be highly dependent on crystal direction, particle size, morphology, roughness, and hydration confined between surfaces. Among the wide range of the surface free energies, the case of water confinement may be closely relevant to the pressure solution creep model as existence of a thin fluid film controls the interface reaction and deformation kinetics.[32] Then, regarding Eq.(1) and relative grain boundary energy measurements, the absolute grain boundary energy of the cold-sintered ZnO is estimated to be small as well, which may closely explain the fast and low-temperature nature of cold sintering. This view agrees with the grain growth energetic study where the activation energy is only 20% of conventional ZnO sintering.[33]
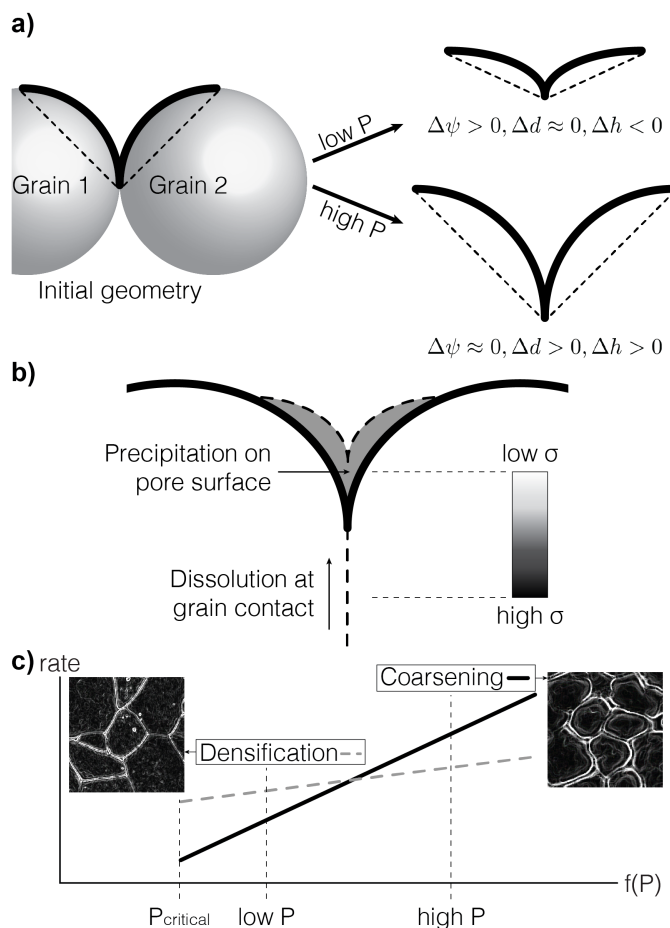
Fig. 3 a) Adjoining grain geometry evolves with respect to applied pressures changing the dihedral angle (ψ), peak-to-peak distance (d), and height (h). b) Pressure-solution creep of adjoining grains under applied pressure where dissolution happens at the grain contact and precipitation occurs at the pore surface and the mass transport follows the local stress gradient (σ). c) Rates of densification and coarsening depend on applied pressure where $P_{critical}$ is a minimal pressure to drive sintering phenomena.

Table 2 Summary of experimental and theoretical calculations of contact angle (θ) and surface free energy (γ_{sv}) of ZnO.

θ [°]	γ_{sv} [J m^{-2}]	Comment
81±4	0.039±0.003	Surface roughness of 175 nm [34]
132 – 154	N/A	Thin film fabricated using (R1) [35]
N/A	4.0	Cleavage energy along c axis [36]
N/A	2.3	Cleavage energy for (1010) surface [36]
N/A	1.31±0.07	Hydrated nanoparticle surface [37]
N/A	2.55±0.23	Anhydrous nanoparticle surface [37]
N/A	0.015–0.053	Water confined between surfaces [38]

Conclusions

Although in-plane microstructure contains distinct information compared to fractography, obtaining a highly flat surface while preserving microstructural features of a cold-sintered sample has been a challenge. Taking ZnO as a model sintering system, this study proposes a method of keeping flat and pristine surface microstructure for understanding topographic evolutions under various pressures. Using the low pressures (70–340 MPa), the interparticle contact was clearly growing while keeping a similar groove geometry. However, the high pressure (475 MPa) rather promotes particle coarsening under confined space. Those observations present that the rates of densification and coarsening depend on uniaxial pressures, which can be an important consideration in controlling microstructure and associated properties. As the surface dihedral angle is a unique morphological attribute, the accurate measurements on the preserved in-plane microstructure certainly contribute to the in-depth understanding of grain growth kinetics and anisotropic energetics of a cold sintering process.

Conflicts of interest

There are no conflicts to declare.

Acknowledgments

Notes and references

1 Z. L. Wang, *Journal of physics: condensed matter*, 2004, **16**, R829.
2 S. C. Pillai, J. M. Kelly, R. Ramesh and D. E. McCormack, *Journal of Materials Chemistry C*, 2013, **1**, 3268–3281.
3 S. Pearton, D. Norton, K. Ip, Y. Heo and T. Steiner, *Superlattices and Microstructures*, 2003, **34**, 3–32.
4 B. Dargatz, J. Gonzalez-Julian and O. Guillon, *Science and technology of advanced materials*, 2015.
5 C. A. Randall, J. Guo, A. Baker, M. Lanagan and G. Hanzheng, *Cold sintering ceramics and composites*, 2017, US Patent App. 15/277,553.
6 A. Serrano, O. Caballero-Calero, M. Á. García, S. Lazić, N. Carmona, G. R. Castro, M. Martín-González and J. F. Fernández, *Journal of the european ceramic society*, 2020, **40**, 5535–5542.
7 C. Spiers and P. Schutjens, *Oil & Gas Science and Technology*, 1999, **54**, 729–750.
8 A. Ndayishimiye, M. Y. Sengul, S. H. Bang, K. Tsuji, K. Takashima, T. H. de Beauvoir, D. Denux, J.-M. Thibaud, A. C. van Duin, C. Elissalde *et al.*, *Journal of the European Ceramic Society*, 2020, **40**, 1312–1324.
9 Y. Yong, M. T. Nguyen, T. Yonezawa, T. Asano, M. Matsubara, H. Tsukamoto, Y.-C. Liao, T. Zhang, S. Isobe and Y. Nakagawa, *Journal of materials chemistry C*, 2017, **5**, 1033–1041.
10 T. H. de Beauvoir, A. Sangregorio, I. Cornu, C. Elissalde and M. Josse, *Journal of Materials Chemistry C*, 2018, **6**, 2229–2233.
11 A. Ndayishimiye, M. Y. Sengul, D. Akbarian, Z. Fan, K. Tsuji, S. H. Bang, A. C. Van Duin and C. A. Randall, *Nano letters*, 2021, **21**, 3451–3457.
12 J. Gonzalez-Julian, K. Neuhaus, M. Bernemann, J. P. da Silva, A. Laptev, M. Bram and O. Guillon, *Acta materialia*, 2018, **144**, 116–128.
13 E. A. Holm and M. E. Chandross, *Determination of Dihedral Angles at Grain Boundary Triple Junctions.*, Sandia national lab.(snl-nm), albuquerque, nm (united states) technical report, 2010.
14 S. H. Bang, A. Ndayishimiye and C. A. Randall, *Journal of Materials Chemistry C*, 2020, **8**, 5668–5672.
15 W. W. Mullins, *Journal of Applied Physics*, 1957, **28**, 333–339.
16 S. H. Bang, K. Tsuji, A. Ndayishimiye, S. Dursun, J. H. Seo, S. Otieno and C. A. Randall, *Journal of the American Ceramic Society*, 2020, **103**, 2322–2327.
17 T. Arii and A. Kishi, *Thermochimica acta*, 2003, **400**, 175–185.
18 B. Dargatz, J. Gonzalez-Julian and O. Guillon, *Journal of crystal growth*, 2015, **419**, 69–78.
19 D. M. Saylor and G. S. Rohrer, *Journal of the American Ceramic Society*, 1999, **82**, 1529–1536.
20 M. N. Kelly, S. A. Bojarski and G. S. Rohrer, *Journal of the American Ceramic Society*, 2017, **100**, 783–791.
21 S. J. Dillon, M. P. Harmer and G. S. Rohrer, *Journal of the American Ceramic Society*, 2010, **93**, 1796–1802.
22 S. A. Bojarski, S. Ma, W. Lenthe, M. P. Harmer and G. S. Rohrer, *Metallurgical and Materials Transactions A*, 2012, **43**, 3532–3538.
23 S. J. Dillon and G. S. Rohrer, *Acta Materialia*, 2009, **57**, 1–7.
24 K. Yanai and M. Hirai, *Journal of the Japan Society of Powder and Powder Metallurgy*, 2000, **47**, 353–363.
25 S.-T. Hong, Y. Hovanski, C. A. Lavender and K. S. Weil, *Journal of Materials Engineering and Performance*, 2008, **17**, 382–386.
26 S. Abdel-Hamid and G. Betz, *Drug development and industrial pharmacy*, 2011, **37**, 387–395.
27 M. Machado, P. Moreira, P. Flores and H. M. Lankarani, *Mechanism and machine theory*, 2012, **53**, 99–121.
28 Y. I. Rabinovich, M. S. Esayanur and B. M. Moudgil, *Langmuir*, 2005, **21**, 10992–10997.
29 M. Y. Sengul, J. Guo, C. A. Randall and A. C. van Duin, *Angewandte Chemie*, 2019, **131**, 12550–12554.
30 P. W. Voorhees, *Journal of Statistical Physics*, 1985, **38**, 231–252.
31 W. J. Khudhayer, R. Sharma and T. Karabacak, *Nanotechnology*, 2009, **20**, 275302.
32 R. van Noort, H. J. Visser and C. J. Spiers, *Journal of Geophysical Research: Solid Earth*, 2008, **113**,.
33 S. Funahashi, J. Guo, H. Guo, K. Wang, A. L. Baker, K. Shiratsuyu and C. A. Randall, *Journal of the American Ceramic Society*, 2017, **100**, 546–553.
34 L. D. Trino, L. F. Dias, L. G. Albano, E. S. Bronze-Uhle, E. C. Rangel, C. F. Graeff and P. N. Lisboa-Filho, *Ceramics International*, 2018, **44**, 4000–4008.
35 N. Tarwal and P. Patil, *Applied surface science*, 2010, **256**, 7451–7456.
36 A. Wander, F. Schedin, P. Steadman, A. Norris, R. McGrath, T. Turner, G. Thornton and N. Harrison, *Physical review letters*, 2001, **86**, 3811.
37 P. Zhang, F. Xu, A. Navrotsky, J. S. Lee, S. Kim and J. Liu, *Chemistry of Materials*, 2007, **19**, 5687–5693.
38 X. Zhang, Z. Shen, J. Liu, S. Kerisit, M. Bowden, M. Sushko, J. De Yoreo and K. M. Rosso, *Nature communications*, 2017, **8**, 1–8.